APPLIED GEOPHYSICS, Vol.19, No. 2 (June 2022), P. 147−160, 15 Figures.
DOI:10.1007/s11770-022-0938-2

A patchy-saturated rock physics model for tight sandstone based on microscopic pore structures

Wu Chun-Fang[1], Ba Jing[1]*, Carcione José M.[1,2], Müller Tobias M.[1], and Zhang Lin[1]

Abstract: The wave-induced local fluid flow mechanism is relevant to the complex heterogeneity of pore structures in rocks. The analysis of the local fluid flow mechanism is useful for accurately describing the wave propagation characteristics in reservoir rocks. In the exploration and production of hydrocarbon reservoirs, the real stratum may be partially saturated with a multi-phase fluid mixture in general. Therefore, it is of great significance to investigate the wave velocity dispersion and attenuation features in relation to pore structures and fluids. In this work, the characteristics of fabric microstructures are obtained on the basis of pressure dependency of dry rock moduli using the effective medium theory. A novel anelasticity theoretical model for the wave propagation in a partially-saturated medium is presented by combining the extended Gurevich squirt-flow model and White patchy-saturation theory. Numerical simulations are used to analyze wave propagation characteristics that depend on water saturation, external patchy diameter, and viscosity. We consider a tight sandstone from the Qingyang area of the Ordos Basin in west China and perform ultrasonic measurements under partial saturation states and different confining pressures, where the basic properties of the rock are obtained at the full gas saturation. The comparison of experimental data and theoretical modeling results shows a fairly good agreement, indicating that the new theory is effective.

Keywords: Pore structure, patchy saturation state, squirt-flow effect, wave velocity dispersion and attenuation

Introduction

The intrinsic wave velocity dispersion and attenuation of sedimentary rocks are widely accepted to be related to the wave-induced local fluid flow mechanisms (WILFF) (Winkler, 1985; Dvorkin et al., 1994; Gist, 1994; Zhao et al., 2010; Ba et al., 2013; Sun et al., 2014; Cheng et al., 2019). The level of wave dispersion and attenuation in real strata is determined by pressures, fluid saturation, fluid contents/types, and pore structures. Additionally, petroleum reservoir exploration and production are aimed at partially-saturated rocks containing two or more immiscible fluid phases. Therefore, the theoretical and experimental studies of wave propagation in partially-saturated rocks are a focus of rock physics research.

Gassmann (1951) studied the effects of pore fluid on the elastic properties without considering the relative motion between the pore fluid and the solid skeleton. Biot (1956a, 1956b, and 1962) developed the fundamental theory of poroelasticity in a fluid-saturated porous solid, which provided the foundation

Manuscript received by the Editor April 6, 2022; revised manuscript received May 12, 2022.
1. School of Earth Sciences and Engineering, Hohai University, Nanjing 211100, China.
2. National Institute of Oceanography and Applied Geophysics (OGS), Trieste 34010, Italy.
*Corresponding author: Ba Jing (Email: jba@hhu.edu.cn)

for simulating wave propagation in a fluid/solid two-phase system and predicted the existence of the slow P-waves. However, the Biot theory is thought to be incapable of explaining the high amplitude degree of wave velocity dispersion and attenuation observed in real rocks (Mavko and Nur, 1975; White, 1975; Dvorkin and Nur, 1993; Carcione, 2014). The Biot theory assumes that the pores are unique or equant (as in a single-porosity medium) and that fluid oscillates/flows only toward wave propagation. These assumptions are inconsistent with the internal complexities of real pore structures. Mavko and Nur (Mavko and Nur, 1975; 1979) considered a squirt-flow mechanism based on pore microscopic geometry, which successfully explained the high wave dispersion and attenuation. However, the theory highly relies on pore geometry. Therefore, this model is difficult to implement and separates the Biot and squirt flows. Mavko and Jizba (1991) proposed the so-called unrelaxed frame for rocks (M–J model), which involves liquid-saturated microcracks and drained stiff pores. The Gassmann equation is then used to calculate the moduli of the fully liquid-saturated rock (in which the dry rock bulk modulus is replaced with the modulus of the unrelaxed frame). The BISQ theory (Dvorkin and Nur, 1993; Dvorkin, 1994) is a more elaborate model that combines the dynamic Biot theory and squirt-flow mechanism. However, the low-frequency P-wave velocity determined by the BISQ model is smaller than that by the Gassmann equation, while it is consistent with the Biot prediction at higher frequencies. Dvorkin et al. (1995) extended the theory to be consistent with the Gassmann equation at low frequencies by assuming effective dry rock moduli and treating microcracks as parts of the skeleton. However, at high frequencies, the P-wave velocity obtained using this model is higher than the high-frequency limit (the prediction by the Biot model without compliant pores) (Wu et al., 2020). According to the effective pressure relaxation approach (Murphy et al., 1986) and the Sayers–Kachanov discontinuity formalism, Gurevich et al. (2009, 2010) extended the model to the arbitrary fluid modulus (Sayers and Kachanov 1995). An extended Gurevich squirt-flow model was proposed by introducing the crack aspect ratio distribution (Deng et al., 2015; Sun et al., 2020; Ouyang et al., 2021). Ba et al. (2011 and 2014) derived a set of the exact equations for acoustic wave propagation in double-porosity rocks containing the mesoscopic heterogeneities based on Hamilton's principle, known as the Biot–Rayleigh equation. Zhang et al. (2017) presented a triple-porosity model for wave propagation in reservoir rocks composed of sand, gravel, and mud components.

The empirical formulas (Brie et al., 1995; Karakul and Ulusay, 2013) and theoretical models (Norris, 1993; Carcione et al., 2003; Toms et al., 2006) have been proposed for analyzing a porous rock saturated with two immiscible fluids with significantly different compressibilities. When the wave frequencies are sufficiently low, the effective fluid modulus in a partially-saturated rock can be estimated by using Wood's law (Wood, 1941). Therefore, with Gassmann's theory, the Gassmann–Wood model (BGW) for a partially-saturated rock was developed. Mavko and Mukerji's (1998) studies clearly demonstrated the model. The predicted bulk modulus of BGW is established when the fluid mixture in the rock is extremely relaxed. Therefore, the predicted BGW result is considered the lower limit of the acoustic wave velocity. Another unrelaxed (stiffened) state occurs when two immiscible fluids are mixed as a patchy-saturation state. At high frequencies, the local fluid pressure does not get enough time to reach the mechanical equilibrium during each wave cycle, causing the rock to "stiffen" during the wave propagation. The modulus of the fluid mixture can be calculated using Hill's (Hill, 1963) theorem. The upper limit of the acoustic wave velocity as a function of saturation will mostly be less than the prediction of the BGH (Biot–Gassmann–Hill) bound (Müller and Gurevich, 2004; Toms et al., 2006).

White (1975) proposed the patchy-saturation theory (the White model) to analyze the wave anelasticity of a mesoscopic patchy-saturation rock model. Dutta and Seriff (1979) reformulated the White mode by using the Biot theory. The predicted P-wave velocity of the reformulated model at the zero-frequency limit is lower than that of the White model and close to the BGW lower limit. The attenuation predicted by the reformulated model is also higher than the White model prediction. Liu et al. (2010) used the White patchy-saturated model to calculate the wave propagation characteristics and analyzed the effects of various fluids on the wave velocity dispersion and attenuation. Ren et al. (2020) proposed a patchy-saturated squirt-flow model based on the Gurevich (2010) model, which considers the single-crack aspect ratio. Li et al. (2018) used the wetting ratio to describe fluid distribution in microcracks/fractures to combine the squirt-flow and patchy-saturation theories in modeling the wave velocities of a partially-saturated rock under different pressures. Sun (2021) proposed a model by incorporating the Biot theory, squirt-flow theory, and mesoscopic dual-porosity theory. However, at low frequencies, the P-wave velocity in predictions is

less than the Gassmann prediction.

In this work, the local fluid flow between microcracks and stiff pores is considered in the patchy-saturation, whereas the interaction between microcracks is neglected. The full gas rock test for the wave velocity dependency of pressure yields the crack aspect ratio distribution under different effective pressures. A novel model is proposed on the basis of the White theory and extended Gurevich squirt-flow model. The experimental data and theoretical results at various water saturation are compared to validate the proposed model's capability to describe the wave anelasticity and characteristics.

Theoretical models

Patchy-saturation (White) model

Patchy-saturation is associated with the spatial distributions of pore structures and fluids, and the patchy size is significantly larger than the grain scale but much smaller than the seismic wavelength. The saturation occurs when some regions with pores are patchy-saturated while the remaining regions are completely saturated on a scale containing many intergranular pores (Mavko and Nolen-Hoeksema, 1994). Two immiscible fluids cause fluid heterogeneity at a mesoscopic scale as waves propagate through the rock, resulting in wave dissipation. Figure 1 shows the White patchy-saturated model (White, 1975), in which concentric spheres aggregate with a gas-filled region embedded in a water-saturated sphere, and the frame assumed to be nearly homogeneous. The sphere inclusion radius is a, the outer radius is b, and $S_g = a^3/b^3$ is the gas saturation. Dutta and Odé (1979) modified the White model to be more exact and rigorous based on the Biot model.

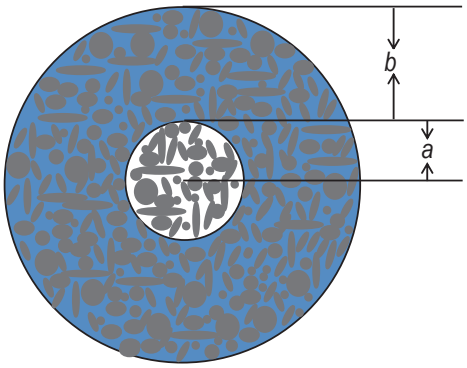

Figure 1. The characteristic element of the White model, where the white and blue areas represent gas- and water-saturated areas, respectively.

Squirt-flow model

Squirt flow occurs when the wave propagates through inhomogeneous rocks because of fluid flow between microcracks and pores (Mavko and Nur, 1975). Gurevich et al. (2010) obtained the dependency of effective moduli on frequency by incorporating the fluid flow effect. Cracks were assumed to have the same crack aspect ratio. Gurevich's (2010) squirt-flow model is then extended to crack aspect ratio distribution (Deng et al., 2015; Sun and Gurevich, 2020; Ouyang et al., 2021). The effective moduli are

$$\frac{1}{K_{wf}} = \frac{1}{K^{hp}} + \sum_{n=1}^{N} \frac{\phi_n}{\frac{4\pi}{3}\frac{\alpha_n \Gamma}{\left(1/K_{dry} - 1/K^{hp}\right)} + \left(\frac{1}{K_f^*} - \frac{1}{K_0}\right)^{-1}}, \quad (1)$$

$$\frac{1}{G_{wf}} = \frac{1}{G_{dry}} - \frac{4}{15}\left(\frac{1}{K_{dry}} - \frac{1}{K_{wf}}\right), \quad (2)$$

$$K_f^* = \left(1 - \frac{2J_1(\lambda)}{\lambda J_0(\lambda)}\right) K_f, \quad (3)$$

$$\lambda = \frac{1}{\alpha_n}\left(-\frac{3i\omega\eta}{K_f}\right)^{1/2}, \quad (4)$$

where K^{hp} is the dry bulk modulus of a hypothetical rock free of microcracks. It can be obtained by fitting the dry rock wave velocity varying with effective pressure (Gurevich et al., 2010). K_{dry} is the dry rock bulk modulus, K_0 is the bulk modulus of the mineral mixture, ϕ_c is microcrack porosity, K_f is the fluid bulk modulus, α_n is the aspect ratio of the n^{th} type of microcracks, ω is the angular frequency, η is fluid viscosity, J_0 and J_1 are the 0^{th} and 1^{st} order Bessel functions, respectively, ϕ_n is the crack porosity of the n^{th} type of microcracks, and Γ is the cumulative crack density. The extended Gurevich squirt-flow model predicts an effective modulus that agrees with the Gassmann equation at the low frequency limit and with the M–J model at the high-frequency limit. The The model also can be used to analyze the influence of the crack aspect ratio distribution on wave velocity dispersion and attenuation. The magnitude of the attenuation peak decreases, the dispersion inflection point and attenuation peak shift to the high-frequency end, and the attenuation frequency range is extended to a broad range (Duan et al., 2017; Sun and Gurevich, 2020; Ouyang et al., 2021).

Once the modified frame moduli are obtained, the moduli of a fully saturated medium can be computed by using the Gassmann equation.

$$K_{sat} = K_{wf} + \frac{\left(1 - K_{wf}/K_0\right)^2}{\phi/K_f + (1-\phi)/K_0 - K_{wf}/K_0^2}, \tag{5}$$

$$G_{sat} = G_{wf}, \tag{6}$$

where ϕ is the total porosity.

The extended Gurevich squirt-flow model

The White model assumes a uniform rock skeleton and that the area outside the inclusion is completely saturated with water. Therefore, in the White model, the effective dry rock moduli (1) and (2) are used for the water-saturated region, while the rock skeleton modulus in the gas-saturated region (region 1) remains constant (Mavko and Nolen-Hoeksema, 1994; Ren et al., 2020). The new model is incorporated into the anelasticity micro- and meso-descriptions. If subindices 1 and 2 refer to the gas-inclusion region and host medium (water-saturated area), respectively, we have the wet rock moduli

$$K(\omega) = \frac{K_\infty}{1 - WK_\infty}, \tag{7}$$

$$G(\omega) = G_{wf}, \tag{8}$$

where

$$K_\infty = \frac{K_{G2}\left(3K_{G1} + 4G_{wf}\right) + 4G_{wf}\left(K_{G1} - K_{G2}\right)S_g}{\left(3K_{G1} + 4G_{wf}\right) - 3\left(K_{G1} - K_{G2}\right)S_g}, \tag{9}$$

$$W = \frac{3ia\kappa\left(R_1 - R_2\right)\left(F_1 - F_2\right)}{b^3\omega\left(\eta_1 Z_1 - \eta_2 Z_2\right)}, \tag{10}$$

with

$$K_{G1} = \frac{K_0 - K_{wf} + \phi K_{wf}\left(K_0/K_{f1} - 1\right)}{1 - \phi - K_{wf}/K_0 + \phi K_0/K_{f1}}, \tag{11}$$

$$K_{G2} = \frac{K_0 - K_{wf} + \phi K_{wf}\left(K_0/K_{f2} - 1\right)}{1 - \phi - K_{wf}/K_0 + \phi K_0/K_{f2}}, \tag{12}$$

are Gassmann moduli, where K_{f1} and K_{f2} are the fluid bulk moduli.

$$R_1 = \frac{\left(K_{G1} - K_{wf}\right)\left(3K_{G2} + 4G_{wf}\right)}{\left(1 - K_{wf}/K_0\right)\begin{bmatrix} K_{G2}\left(3K_{G1} + 4G_{wf}\right) \\ +4G_{wf}\left(K_{G1} - K_{G2}\right)S_g \end{bmatrix}}, \tag{13}$$

$$R_2 = \frac{\left(K_{G2} - K_{wf}\right)\left(3K_{G1} + 4G_{wf}\right)}{\left(1 - K_{wf}/K_0\right)\begin{bmatrix} K_{G2}\left(3K_{G1} + 4G_{wf}\right) \\ +4G_{wf}\left(K_{G1} - K_{G2}\right)S_g \end{bmatrix}}, \tag{14}$$

$$F_1 = \frac{\left(1 - K_{wf}/K_0\right)K_{A1}}{K_{G1}}, \tag{15}$$

$$F_2 = \frac{\left(1 - K_{wf}/K_0\right)K_{A2}}{K_{G2}}, \tag{16}$$

$$Z_1 = \frac{1 - \exp\left(-2\gamma_1 a\right)}{\left(\gamma_1 a - 1\right) + \left(\gamma_1 a + 1\right)\exp\left(-2\gamma_1 a\right)}, \tag{17}$$

$$Z_2 = \frac{\left(\gamma_2 b + 1\right) + \left(\gamma_2 b - 1\right)\exp\left[-2\gamma_2\left(b - a\right)\right]}{\left(\gamma_2 b + 1\right)\left(\gamma_2 a - 1\right) - \left(\gamma_2 b - 1\right)\left(\gamma_2 a + 1\right)} - \exp\left[-2\gamma_2\left(b - a\right)\right], \tag{18}$$

$$\gamma_1 = \sqrt{i\omega\eta_1/\kappa K_{E1}}, \tag{19}$$

$$\gamma_2 = \sqrt{i\omega\eta_2/\kappa K_{E2}}, \tag{20}$$

where η_1 and η_2 are fluid viscosities, and

$$K_{E1} = \left[1 - \frac{K_{f1}\left(1 - K_{G1}/K_0\right)\left(1 - K_{wf}/K_0\right)}{\phi K_{G1}\left(1 - K_{f1}/K_0\right)}\right]K_{A1}, \tag{21}$$

$$K_{E2} = \left[1 - \frac{K_{f2}\left(1 - K_{G2}/K_0\right)\left(1 - K_{wf}/K_0\right)}{\phi K_{G2}\left(1 - K_{f2}/K_0\right)}\right]K_{A2}, \tag{22}$$

$$\frac{1}{K_{A1}} = \left(\frac{\phi}{K_{f1}} + \frac{1-\phi}{K_0} - \frac{K_{wf}}{K_0^2}\right), \tag{23}$$

$$\frac{1}{K_{A2}} = \left(\frac{\phi}{K_{f2}} + \frac{1-\phi}{K_0} - \frac{K_{wf}}{K_0^2}\right). \tag{24}$$

According to Wood (1941), the effective bulk modulus of the gas-water mixture is

$$\frac{1}{K_f} = \frac{S_g}{K_{f1}} + \frac{S_w}{K_{f2}}, \tag{25}$$

where S_w is the water saturation.

Finally, the P-wave phase velocity and attenuation are

$$V_p = \sqrt{\frac{\mathrm{Re}\left(K(\omega)+4G(\omega)/3\right)}{\rho}}, \tag{26}$$

$$Q_p^{-1} = \frac{\mathrm{Im}\left(K(\omega)+4G(\omega)/3\right)}{\mathrm{Re}\left(K(\omega)+4G(\omega)/3\right)}, \tag{27}$$

where $\rho=(1-\phi)\rho_s+\phi\left(S_g\rho_1+S_w\rho_2\right)$ is the bulk density, ρ_s is the solid density, ρ_1 and ρ_2 are the fluid densities.

Low and high frequency limits of P-wave velocity in partially saturated rocks

As the frequency is low enough, the rock is relaxed. The effective modulus of the pore fluid is given by Wood's law, which is exact for the static modulus of two immiscible fluids. As the frequency is high enough, the rock is "stiffened" during the wave propagation. In such a situation Hill's theorem is an exact result for the effective bulk modulus of the composite. Therefore, the predicted result of Gassmann-Wood and Gassmann-Hill are considered as the lower and upper limits of the acoustic wave velocity as a function of saturation in the partially saturated rock, respectively (Müller and Gurevich, 2004; Toms et al., 2006).

Numerical examples

Results of models

Results of this study model, White model and White-Squirt model, are compared based on the same rock properties, which are listed in Table 1.

Table 1. Physical parameters used in this study model

Parameter (units)	Value	Parameter (units)	Value
Mineral density (kg/m^3)	2650	Water bulk modulus (GPa)	2.25
Mineral mixture bulk modulus (GPa)	38	Gas bulk modulus (GPa)	0.0022
Dry rock bulk modulus (GPa)	17	Water density (kg/m^3)	1000
Dry rock shear modulus (GPa)	12.6	Gas density (kg/m^3)	1.2
Permeability (mD)	1	Water viscosity (Pa·s)	0.001
Porosity (%)	10	Gas viscosity (Pa·s)	0.0001
External patchy diameter (m)	0.01	Microcrack aspect ration	0.001~ 0.00001
Water saturation	0.8		

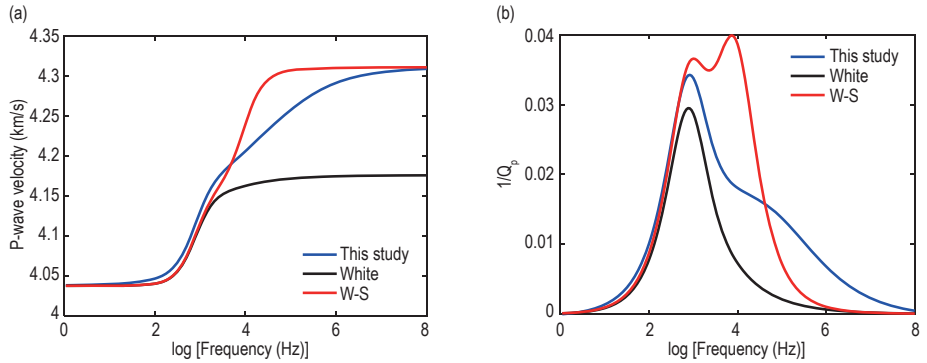

Figure 2. P-wave velocity (a) and attenuation (b) by the models.

The results are shown in Figure 2. The W–S model is the White patchy-saturated squirt-flow model proposed by Ren et al. (2020) based on the Gurevich (2010) and the White models. Figure 2a shows that the P-wave wave velocities computed by the three models are the same at low frequencies (about less than 50 Hz), whereas the P-wave wave velocity computed by this study is greater than the White prediction at the high-frequency limit, which is consistent with the W–S model results. The P-wave attenuation by the new model is greater than that of the White model in Figure 2b. The attenuation from the W-S model becomes zero, whereas the new model still has high attenuation at high frequencies (about more than 10 MHz). Therefore, the new model's attenuation occurs over a wide frequency range. The main reason for this is that the new model can be used to calculate the

effect of the squirt flow between cracks with different aspect ratios.

Effect of water saturation

The influence of water saturation and frequency on the wave propagation characteristics is analyzed within the water saturation range from 0 to 1, and the remaining properties are listed in Table 1. Figure 3 shows the wave propagation characteristics. The P-wave velocity increases with the increase of frequency, and it increases first and then decreases as the water saturation increases. The dispersion and attenuation reach their maximum values when the water saturation is around 80%. The two attenuation peaks tend to split in the high water saturation range. The main reason is that, with the increase in water saturation, the attenuation peak caused by the mesoscale heterogeneity moves to the low-frequency end, while the peak caused by the microscale heterogeneity remains constant.

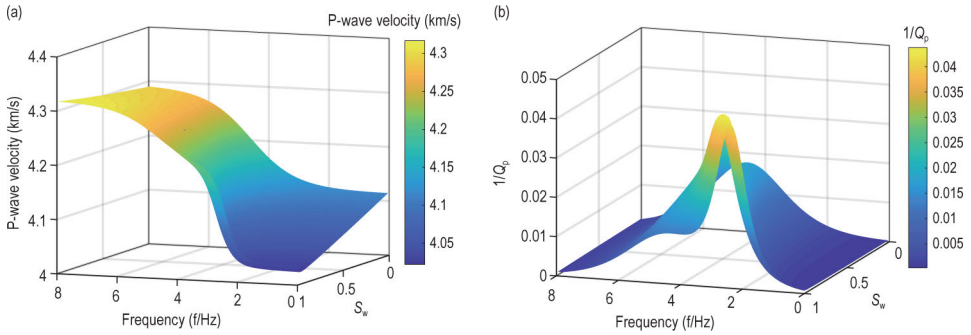

Figure 3. P-wave velocity (a) and attenuation (b) as a function of water saturation and frequency.

Effect of external patchy diameter

Figure 4 shows P-wave velocity and attenuation as a function of external patchy diameter and frequency. Table 1 lists the other properties and the external patchy diameter, which is in the range of 0.01–0.04 m. When the radius of the outer sphere increases, the P-wave velocity dispersion becomes more significant, and the characteristic frequency moves to low frequencies. The characteristic frequency of the squirt flow remains constant. Consequently, when the external patchy diameter increases, there are two attenuation peaks (Liu et al., 2010).

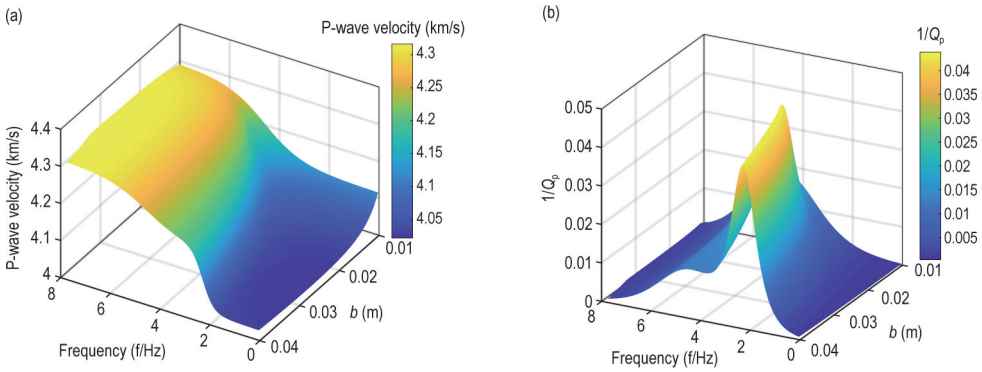

Figure 4. P-wave velocity (a) and attenuation (b) as a function of external patchy diameter and frequency.

Effect of viscosity

Figure 5 shows P-wave velocity and attenuation as a function of fluid viscosity of region 2 and frequency. The viscosity is in the range of 0.001–0.01 Pa·s, and the other properties are listed in Table 1. The attenuation peak moves to low frequency with the increase of viscosity.

Model applications

Ultrasonic data

A tight sandstone from the Qingyang area of the Ordos Basin is considered. The sample (S) is formed into a cylinder with an approximate diameter of 25.1 mm

and a height of 50 mm, and the core ends are polished. An aluminum cylinder with the same shape and size was prepared as the reference standard. The sample is composed of quartz, feldspar, and interstitial materials (mainly carbonate minerals and clay), with a porosity of 5.79%. Figure 6 shows the cast thin section analyses regarding the sample. The experimental setup consists of a pulse generator, a temperature control unit, a confining pressure control unit, a pore pressure control unit, and an ultrasonic wave test unit (Guo et al., 2009; Yan et al., 2011; Ma and Ba, 2020).

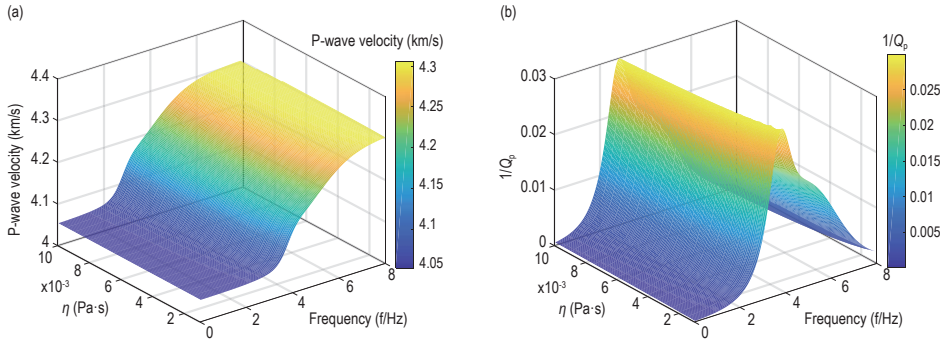

Figure 5. P-wave velocity (a) and attenuation (b) as a function of fluid viscosity and frequency.

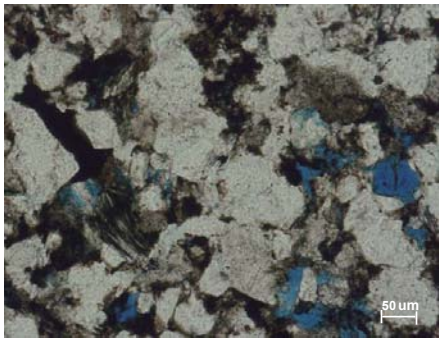

Figure 6. Thin section image of the tight sandstone.

The piezoelectric ultrasonic wave transducers were placed at the top and bottom of the sample. The rubber sleeve is used to seal the sample. An electrical pulse is applied to the source transducer to generate the ultrasonic P-waves. A digital oscilloscope is used to display and record the waveforms from the receiver. The appropriate units control the temperature, pore pressure, and confining pressure (Ma and Ba, 2020). The pore pressure is 15 MPa, the effective pressures are 5, 15, 25, 35, and 45 MPa, the temperature is 20°C, and the waveforms are recorded after the experimental conditions have been maintained for 30 mins. The samples for the partial gas(air)-water saturation tests are first saturated with water using the vacuum pressure saturation method before being placed in an oven to vary the saturation. The approach of Ba et al. (2019) is adopted to quantify the fluid content. The sample is tested at six different levels of water saturation (0%, 20%, 40%, 60%, 80%, and 100%). The wave velocities are calculated from the travel times, and the spectral-ratio method is used to obtain the dissipation factor.

Figure 7 shows the gas-water partially-saturated rock wave velocities as a function of effective pressure are presented. The P-wave velocities gradually increase from dry to fully saturated conditions under different pressures (see Figure 7a). As expected, the P-wave velocity increases with water saturation and confining pressure, showing an approximately linear trend at the

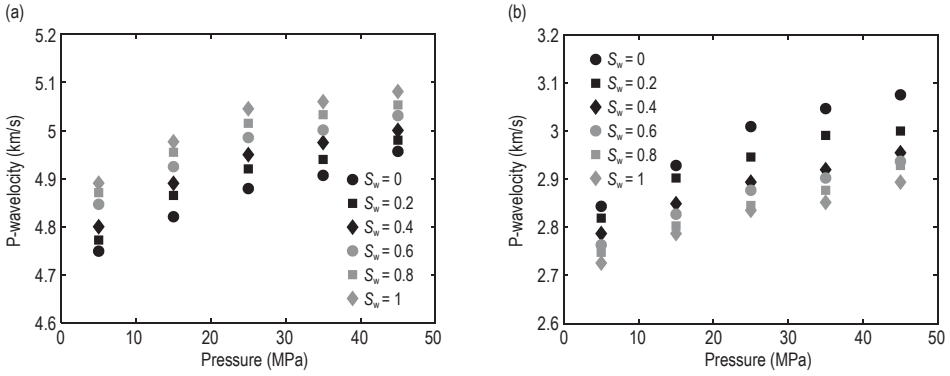

Figure 7. P-wave velocity (a) and S-wave velocity (b) as a function of effective pressure at different water saturations.

high pressures (Deng et al., 2015; Song et al., 2015) due to some of the closed microcracks. In the gas-water partially-saturated rock, the pore spaces contain gas and water. The water bulk modulus is higher than that of gas. As water saturation increases, the volume ratio of air decreases, and that of water increases while the rock skeleton remains constant. Generally, the P-wave velocity increases with increasing water saturation. The effect of effective pressure on the stiff pores is minor and can be neglected (Chen et al., 2009; David and Zimmerman, 2012; Deng et al., 2015). The S-wave velocity also increases with the effective pressure but decreases as saturation increases due to the effect of density (see Figure 7b).

The dissipation factor can be obtained using the spectral-ratio method and a high-quality reference standard material (Lucet and Zinszner, 1992; Guo and Fu, 2006; Picotti and Carcione, 2006; Ba et al., 2019; Ma and Ba, 2020) from

$$\ln\left(\frac{A_1(f)}{A_2(f)}\right) = -\frac{\pi x}{Q\,V} f + \ln\frac{G_1(x)}{G_2(x)}, \qquad (28)$$

where f is the frequency, $A_1(f)$ and $A_2(f)$ are the amplitude spectra of the rock sample and aluminum standard, respectively, Q denotes the rock sample's quality factor, x is the propagation distance, V is the wave velocity in the rock sample, and $G_1(x)$ $G_2(x)$ are the sample and standard geometrical factors, respectively.

Figure 8 shows how the attenuation decreases with effective pressure. The variations in attenuation with respect to effective pressure and saturation are similar to those of the sandstone samples analyzed by Amalokwu et al. (2017) and Pang et al. (2020).

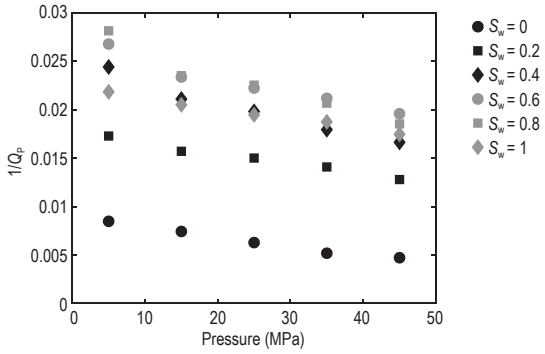

Figure 8. P-wave attenuation as a function of effective pressure and saturation.

The microcrack porosity and cumulative microcrack density are obtained based on the experimental data. The estimation method is given in Appendix A. Figure 9 shows the sample distribution curves under different pressures. The value of the microcrack aspect ratio exhibits a continuous spectrum within a certain range (Deng et al., 2015; Zhang et al., 2019; Sun et al., 2020). Therefore, the microcrack porosity and cumulative microcrack density are shown as a continuous spectrum within a certain range.

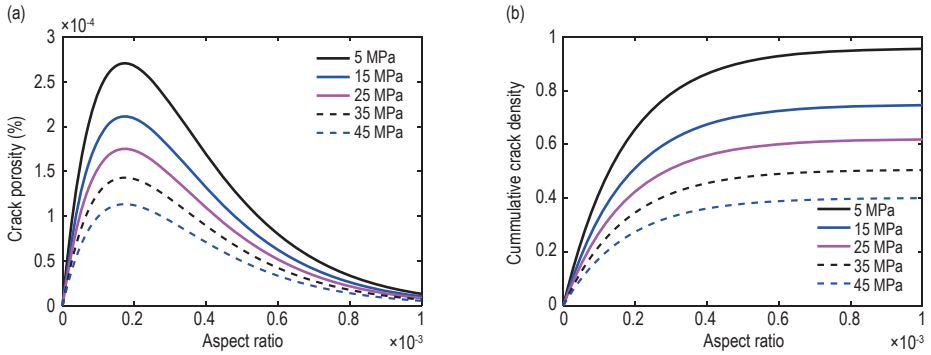

Figure 9. The microcrack porosity distribution function (a) and cumulative microcrack porosity with respect to the aspect ratio for the tight sandstone.

P-wave velocity dispersion and attenuation

The proposed model is used to predict the P-wave velocity and attenuation of sample S at 5 MPa effective pressure. The dry rock bulk modulus is 26.2 GPa, the Poisson ratio is 0.15, the permeability is 0.02 mD, the outer diameter is 0.02 m, and the fluid properties are obtained using the Batzle and Wang measurement conditions (1992). Figure 10 compares the results for different models. The Gassmann–Hill curve does not consider the wave-induced fluid flow mechanisms. When the water saturation is low, the P-wave velocities computed by the proposed model and the White model are both located within the limits of the Gassmann–Wood and Gassmann–Hill equations. The P-wave velocity computed by the proposed model exceeds the upper limit of the Gassmann–Hill equation with the increase in water saturation. The presented model incorporates

the influences of the mesoscopic and microscopic fluid flows. The microscopic fluid flow mechanism stiffens the rock skeleton as water saturation increases, resulting in the velocity increase. When the water saturation exceeds 60%, the P-wave velocity exceeds the upper limit of the Gassmann–Hill equation (Ba et al., 2016), which does not incorporate the stiffening effect of rock skeleton by the microscopic fluid flow.

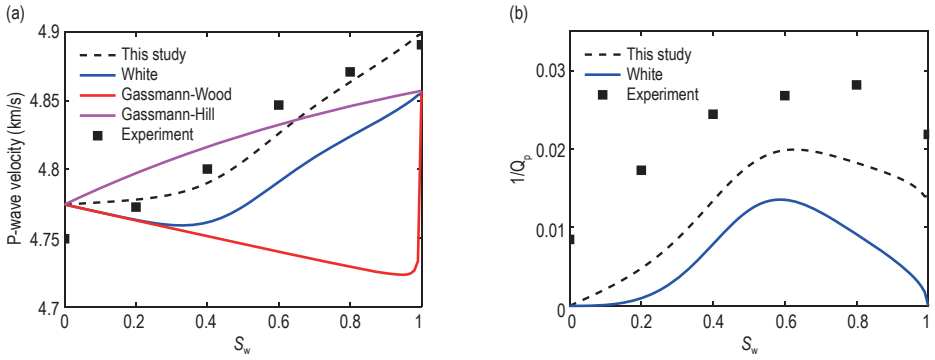

Figure 10. P-wave velocity (a) and attenuation (b) as a function of water saturation at 5 MPa.

The fluid pressure gradient between the different regions determines the attenuation in the White patchy saturation model. Fluid flow is confined to the area near the interface of fluid regions at high frequencies, and fluid exchange is related to the fluid pressure gradient and the contact area. There is critical water saturation in partially-saturated rocks. When the water saturation is less than that of the critical value, the attenuation increases as water saturation increases. When it exceeds the critical value, the attenuation decreases with increasing water saturation. The attenuation reaches the maximum at the critical water saturation. The critical saturation is about 60% at the pressure of 5 MPa (see Figure 10b). The trend is similar to those of the sandstone samples analyzed by Amalokwu et al. (2017).

In the example, Figures 11–14 show the P-wave velocity and attenuation as a function of water saturation at four different pressures (15, 25, 35, and 45 MPa). Generally, the trend is similar to that observed at 5 MPa. As the pressure rises, the P-wave velocity predictions by

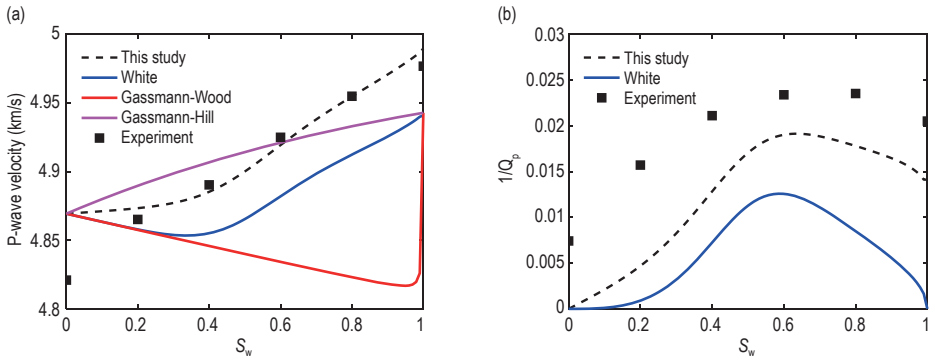

Figure 11. P-wave velocity (a) and attenuation (b) as a function of water saturation at 15 MPa.

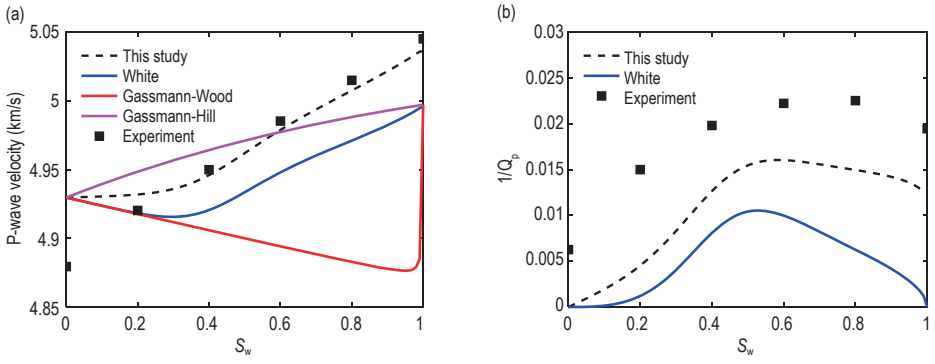

Figure 12. P-wave velocity (a) and attenuation (b) as a function of water saturation at 25 MPa.

the proposed model increase, and the critical saturation tends to shift to the low saturation end (Ren et al., 2020).

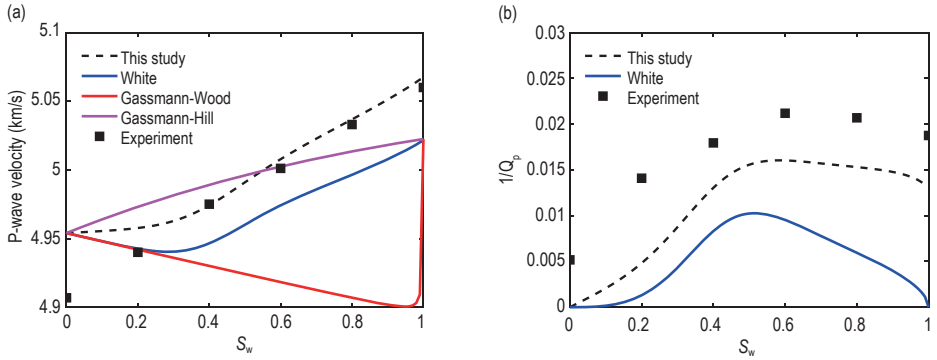

Figure 13. P-wave velocity (a) and attenuation (b) as a function of water saturation at 35 MPa.

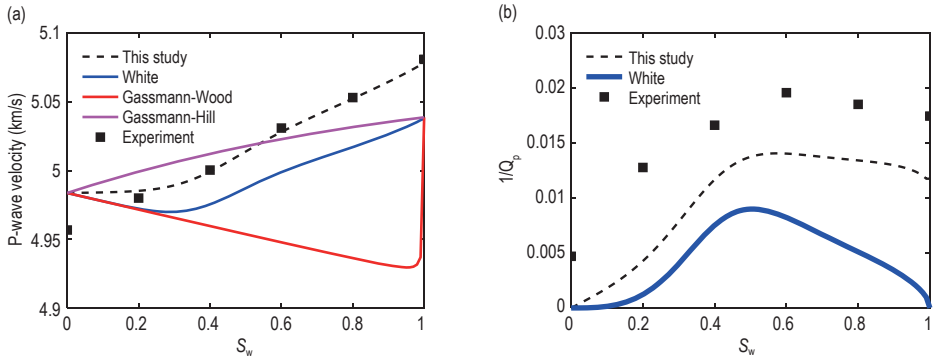

Figure 14. P-wave velocity (a) and attenuation (b) as a function of water saturation at 45 MPa.

Compare predicted results and the experiments

Figure 15 shows the crossplots of the measured and predicted velocities and attenuation. The P-wave velocities demonstrate a good agreement. The attenuation predicted by the presented model is less than the measured one. The main reason for this is that the model mainly considers the mesoscopic loss caused by partial saturation. Additional attenuation may occur due to the presence of multiple minerals and the clay content and distribution (Picotti and Carcione, 2006; Chen et al., 2009).

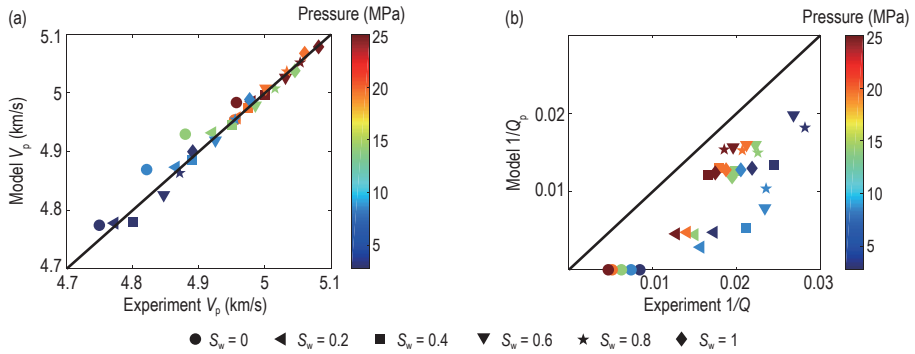

Figure 15. Comparison of the measured and predicted velocities (a) and attenuation (b) at different water saturations.

Conclusions

A model for describing the wave anelasticity in partially-saturated rocks is proposed by combining the White theory and extended Gurevich squirt-flow model and incorporating the effects of microcrack aspect ratio distribution. The microcrack properties are obtained with the experimental data at the different effective pressures and water saturations. We compare the results with those of the White model and W-S model, showing that the proposed model provides a good agreement between

theoretical predictions and experimental data for tight sandstones, mainly the P-wave velocity dependence of saturation and effective pressure. The range of transition zone between the low- and high-frequency limits (the relaxation frequency) for the dispersion curves is broader. The wave velocity dispersion and attenuation computed by the proposed model and the White model are similar at low water saturations. The effect of squirt-flow is enhanced as water saturation increases, and the dispersion and attenuation predicted by the proposed model are greater than those by the White model. When the water saturation is high and the external patchy diameter is large, the frequency of attenuation peak (related to mesoscopic heterogeneity) shifts to the low-frequency end, while the frequency of attenuation peak (related to microscopic heterogeneity) remains constant. There are two attenuation peaks according to the proposed model. The combined effect of patchy saturation and squirt-flow mechanisms in the seismic interpretation will help to develop multi-frequency rock physics modeling of the target formations. It will help in inverting the properties of underground rocks in field applications by combining ultrasonic measurements, well logging data, and seismic attribute observations.

Moreover, a better description at high frequencies (e.g., in the ultrasonic frequency range) should include the Biot attenuation peak. The model's generalization will require additional work. Due to the complex microstructures and fabric heterogeneity of the tight sandstones, the proposed model is still incapable of fully describing the experimental measurement data, particularly at low effective pressures.

Acknowledgments

This work is supported by the National Natural Science Foundation of China (Grant no. 41704109) and the Jiangsu Province Outstanding Youth Fund Project (Grant no. BK20200021).

References

Amalokwu, K., Papageorgiou, G., Chapman, M., and Best, A. I., 2017, Modelling ultrasonic laboratory measurements of the saturation dependence of elastic modulus: New insights and implications for wave propagation mechanisms: International Journal of Greenhouse Gas Control, **59**, 148–159.

Ba, J., Carcione, J. M., and Nie, J. X., 2011, Biot-Rayleigh theory of wave propagation in double-porosity media: Journal of Geophysical Research: Solid Earth, **116**, B06202.

Ba, J., Yan, X. F., Chen, Z. Y. et al., 2013, Rock physics model and gas saturation inversion for heterogeneous gas reservoirs: Chinese Journal of Geophysics (in Chinese), **56**(5), 1696–1706.

Ba, J., Zhang, L., Sun, W. T., and Hao, Z. B., 2014, Velocity field of wave-induced local fluid flow in double-porosity media: Science China: Physics, Mechanics and Astronomy, **57**, 1020–1030.

Ba, J., Zhao, J., Carcione, J. M. et al., 2016, Compressional wave dispersion due to rock matrix stiffening by clay squirt-flow: Geophysical Research Letters, **43**(12), 6186–6195.

Ba, J., Ma, R. P., Carcione, J. M., and Picotti, S., 2019, Ultrasonic wave attenuation dependence on saturation in tight oil siltstones: Journal of Petroleum Science and Engineering, **179**, 1114–1122.

Batzle, M., and Wang, Z., 1992, Seismic properties of pore fluids: Geophysics, **57** (11), 1396–1408.

Berryman, J. G., 1995, Mixture theories for rock properties, A Handbook of Physical Constants: Washington, D. C: American Geophysical Union, 205–228.

Biot, M. A., 1956a, Theory of propagation of elastic waves in a fluid-saturated porous solid. I. Low frequency range: The Journal of the Acoustical Society of America, **28**(2), 168–178.

Biot, M. A., 1956b, Theory of propagation of elastic waves in a fluid- saturated porous solid. II. Higher frequency range: The Journal of the Acoustical Society of America, **28**(2), 179–191.

Biot, M. A., 1962, Generalized theory of acoustic propagation in porous dissipative media: The Journal of the Acoustical Society of America, **34**(9A), 1254–1264.

Brie, A., Pampuri, F., Marsala, A. F., and Meazza, O., 1995, Shear sonic interpretation in gas-bearing sands: SPE Annual Technical Conference and Exhibition, October, Dallas, USA, SPE 30595, 701–710.

Carcione, J. M., 2014, Wave fields in real media. Theory and numerical simulation of wave propagation in anisotropic, anelastic, porous and electromagnetic media, 3rd ed.: Elsevier, Amsterdam.

Carcione, J. M., Helle, H. B., and Pham, N. H., 2003, White's model for wave propagation in partially saturated rocks: comparison with poroelastic numerical experiments: Geophysics, **68**(4), 1389–1398.

Chen, Y., Huang, T. F., and Liu, E. R., 2009, Rock Physics (in Chinese): China University of Science and Technology Press, Hefei.

Cheng, W., Ba, J., Fu, L. Y. et al., 2019, Wave-velocity dispersion and rock microstructure: Journal of Petroleum Science and Engineering, **183**, 106466.

David, E. C., and Zimmerman, R. W., 2012, Pore structure model for elastic wave velocities in fluid-saturated sandstones: Journal of Geophysical Research: Solid Earth, **117**, B07210.

Deng, J. X., Zhou, H., Wang, H. et al., 2015, The influence of pore structure in reservoir sandstone on dispersion properties of elastic waves: Chinese Journal of Geophysics (In Chinese), **58**(9), 3389–3400.

Duan, C. S., Deng, J. X., Li, Y. et al., 2017, Effect of pore structure on the dispersion and attenuation of fluid-saturated tight sandstones: Journal of Geophysics and Engineering, **15**(2018), 449–460.

Dutta, N. C., and Odé, H., 1979, Attenuation and dispersion of compressional waves in fluid-filled porous rocks with partial gas saturation (White model)-Part I: Biot theory: Geophysics, **44**, 1777–1788.

Dutta, N. C., and Seriff, A. J., 1979, On White′s model of attenuation in rocks with partial gas saturation: Geophysics, **44**(11), 1806–1812.

Dvorkin, J., Mavkon, G., and Nur, A., 1995, Squirt-flow in fully saturated rocks: Geophysics, **60**(1), 97–107.

Dvorkin, J., and Nur, A., 1993, Dynamic poroelasticity: a unified model with the squirt and the Biot mechanics: Geophysics, **58**(4), 524–533.

Dvorkin, J., Nolen-Hoeksema, R., and Nur, A., 1994, The squirt-flow mechanism: macroscopic description: Geophysics, **59**(3), 428–438.

Gassmann, F., 1951, Über die elastizität poröser medien: Vierteljahrsschrift der Naturforschenden Gesellschaft in Zürich, **96**, 1–23.

Gist, G. A., 1994, Interpreting laboratory velocity measurements in partially gas-saturated rocks: Geophysics, **59**, 1100–1109.

Guo, M., and Fu, Y., 2006, Stress associated coda attenuation from ultrasonic waveform Measurements: Geophysical Research Letters, **34**, L09307.

Guo, M. Q., Fu, L. Y., and Ba, J., 2009, Comparison of stress-associated coda attenuation and intrinsic attenuation from ultrasonic measurements: Geophysical Journal International, **178**, 447–456.

Gurevich, B., Makarynska, D., and Pervukhina, M., 2009, Ultrasonic moduli for fluid-saturated rocks: Mavko-Jizba relations rederived and generalized: Geophysics, **74**(4), N25–N30.

Gurevich, B., Makarynska, D., de Paula, O. B. et al., 2010, A simple model for squirt-flow dispersion and attenuation in fluid-saturated granular rocks: Geophysics, **75**(6), N109–N120.

Hill, R., 1963, Elastic properties of reinforced solids: some theoretical principles: Journal of the Mechanics and Physics of Solids, **11**, 357–372.

Karakul, H., and Ulusay, R., 2013, Empirical correlations for predicting strength properties of rocks from P-wave velocity under different degrees of saturation: Rock Mechanics & Rock Engineering, **46**(5), 981–999.

Li, D. Q., Wei, J. X., Di, B. R. et al., 2018, Experimental study and theoretical interpretation of saturation effect on ultrasonic velocity in tight sandstones under different pressure conditions: Geophysical Journal International, **212**(3), 2226–2237.

Liu, J., Ma, J. W., and Yang, H. Z., 2010, Research on P-wave′s propagation in White′s sphere model with patchy saturation: Chinese Journal of Geophysics (in Chinese), **53**(4), 954–962.

Lucet, N., and Zinszner, B., 1992, Effects of heterogeneities and anisotropy on sonic and ultrasonic attenuation in rocks: Geophysics, **57**(8), 1018–1026.

Ma, R. P., and Ba, J., 2020, Coda and intrinsic attenuations from ultrasonic measurements in tight siltstones: Journal of Geophysical Research: Solid Earth, **125**, e2019JB018825.

Mavko, G., and Jizba, D., 1991, Estimating grain-scale fluid effects on velocity dispersion in rocks: Geophysics, **56**(12), 1940–1949.

Mavko, G., and Nur, A., 1975, Melt squirt in the asthenosphere: Journal of Geophysical Research, **80**, 1444–1448.

Mavko, G., and Nur, A., 1979, Wave attenuation in partially saturated rocks: Geophysics, **44**(2): 161-178.Mavko, G., and Nolen-Hoeksema, R., 1994, Estimating seismic velocities at ultrasonic frequencies in partially saturated rocks: Geophysics, **59**(2), 252–258.

Mavko, G., and Mukerji, T., 1998, Bounds on low-frequency seismic velocities in partially saturated rocks: Geophysics, **63**(3), 918–924.

Murphy, W. F., Winkler, K. W., and Kleinberg, R. L., 1986, Acoustic relaxation in sedimentary rocks: dependence on grain contacts and fluid saturation: Geophysics, **51**(3), 757–766.

Müller, T. M., and Gurevich, B., 2004, One-dimensional random patchy saturation model for velocity and attenuation in porous rocks: Geophysics, **69**, 1166–1172.

Norris, A. N., 1993, Low-frequency dispersion and attenuation in partially saturated rocks: Journal of the Acoustical Society of America, **94**(1), 359–370.

Ouyang, F., Zhao, J. G, Li, Z. et al., 2021, Modeling velocity dispersion and attenuation using pore structure characteristics of rock: Chinese Journal of Geophysics (In Chinese), **64**(3), 1034–1047.

Pang, M. Q. Ba, J. Ma, R. P., and Chen, T. S., 2020, Analysis of attenuation rock-physics template of tight sandstones: Reservoir microcrack prediction: Chinese Journal of Geophysics (In Chinese), **63**, 281–295.

Picotti, S., and Carcione, J. M., 2006, Estimating seismic attenuation (Q) in the presence of random noise: Journal of Seismic Exploration, **15**, 165–181.

Ren, S. B., Han, T. C., and Fu, L. Y., 2020, Theoretical and experimental study of P-wave attenuation in partially saturated sandstones under different pressures: Chinese Journal of Geophysics (in Chinese), **63**(7), 2722–2736.

Sayers, C. M., and Kachanov, M., 1995, Microcrack-induced elastic wave anisotropy of brittle rocks: Journal of Geophysical Research Solid Earth, **100**(B3), 4149–4156.

Sun, W. T., Ba, J., Müller, T. M. et al., 2014, Comparison of P-wave attenuation models of wave-induced flow: Geophysical Prospecting, **63**(2), 378–390.

Sun, Y., Carcione J. M., and Gurevich, B., 2020, Squirt-flow seismic dispersion models: a comparison: Geophysical Journal International, **222**(3), 2068–2082.

Sun, Y., and Gurevich, B., 2020, Modeling the effect of pressure on the moduli dispersion in fluid-saturated rocks: Journal of Geophysical Research: Solid Earth, **125**(12), e2019JB019297.

Sun, C., Tang, G., Fortin, J. et al., 2020, Dispersion and attenuation of elastic wave velocities: impact of microstructure heterogeneity and local measurements: Journal of Geophysical Research: Solid Earth, **125**(12) e2020JB020123.

Sun, W. T., 2021, On the theory of Biot-patchy-squirt mechanism for wave propagation in partially saturated double-porosity medium: Physics Fluids, **33**, 076603.

Song, L. T, Wang, Y., Liu, Z. H. et al., 2015, Elastic anisotropy characteristics of tight sands under different confining pressures and fluid saturation states: Chinese Journal of Geophysics (in Chinese), **58**(9), 3401–3411.

Tang X. M., Wang H. M., Sun Y. D. et al., 2021, Inversion for micro-pore structure distribution characteristics using cracked porous medium elastic wave theory. Chinese Journal of Geophysics (In Chinese), **64**(8), 2941–2951.

Toms, J., Müller, T. M., Ciz, R., and Gurevich, B., 2006, Comparative review of theoretical models for elastic wave attenuation and dispersion in partially saturated rocks: Soil Dynamics and Earthquake Engineering, **26**(6–7), 548–565.

White, J. E., 1975, Computed seismic speeds and attenuation in rocks with partial gas saturation: Geophysics, **40**(2), 224–232.

Winkler, K. W., 1985, Dispersion analysis of velocity and attenuation in Berea sandstone. Journal of Geophysical Research: Solid Earth, **90**(B8), 6793–6800.

Wood, A. B., 1941, A Textbook of Sound, Bell: London, UK.

Wu, C. F., Ba, J., Carcione, J. M., Fu, L. Y. Chesnokov, E. M., and Zhang, L., 2020, A squirt-flow theory to model wave anelasticity in rocks: Physics of the Earth and Planetary Interiors, **301**, 106450.

Yan, X. F., Yao, F. C., Cao, H. et al., 2011, Analyzing the mid-low porosity sandstone dry frame in central Sichuan based on effective medium theory: Applied Geophysics, **8**(3), 163–170.

Zhang, L, Ba, J, Fu, L. Y., et al., 2019, Estimation of pore microstructure by using the static and dynamic moduli: International Journal of Rock Mechanics and Mining Sciences, **113**, 24–30.

Zhang, L., Ba, J., Yin, W. et al., 2017, Seismic wave propagation equations of conglomerate reservoirs: A triple-porosity structure model: Chinese Journal of Geophysics (In Chinese), **60**(3), 1073–1087.

Zhao, H. B., Wang, X. M., Chen, S. M. et al., 2010, Acoustic response characteristics of unsaturated porous media. Science China Physics, Mechanics and Astronomy, **53**(8), 1388–1396.

Appendix A

Microcrack porosity and cumulative microcrack density estimation at different effective pressures

Step 1: The aspect ratio of the stiff pores is estimated. Based on the MT model (Mori and Tanaka), the quantitative relation between elastic moduli and stiff porosity is established. The effective moduli are

$$\frac{1}{K_{stiff}^{MT}} = \frac{1}{K_0}\left(1+\frac{\phi_s}{1-\phi_s}M\right), \tag{A1}$$

$$\frac{1}{G_{stiff}^{MT}} = \frac{1}{G_0}\left(1+\frac{\phi_s}{1-\phi_s}N\right), \tag{A2}$$

where K_{stiff}^{MT} and G_{stiff}^{MT} are the bulk and shear moduli of the host material, respectively, G_0 is the shear modulus, and ϕ_s is stiff porosity. M and N are the shape factors

of stiff pores, which are related to the aspect ratio of ellipsoidal pores and the Poisson ratio of rock grains (Berryman, 1995).

Microcracks are embedded into the host material by neglecting the interactions between microcracks and stiff pores. The effective moduli are

$$\frac{1}{K_{eff}^{MT}}=\frac{1}{K_{stiff}^{MT}}\left(1+\frac{16\left(1-\left(\upsilon_{stiff}^{MT}\right)^{2}\right)\Gamma}{9\left(1-2\upsilon_{stiff}^{MT}\right)}\right), \tag{A3}$$

$$\frac{1}{G_{eff}^{MT}}=\frac{1}{G_{stiff}^{MT}}\left(1+\frac{32\left(1-\upsilon_{stiff}^{MT}\right)\left(5-\upsilon_{stiff}^{MT}\right)\Gamma}{45\left(2-\upsilon_{stiff}^{MT}\right)}\right), \tag{A4}$$

where $\upsilon_{stiff}^{MT}=\left(3K_{stiff}^{MT}-2\mu_{stiff}^{MT}\right)/\left(6K_{stiff}^{MT}+2\mu_{stiff}^{MT}\right)$, K_{eff}^{MT} and G_{eff}^{MT} are the effective bulk and shear moduli, respectively, when the rock contains microcracks and stiff pores. All the microcracks tend to close at the high effective pressure range so that there remain only stiff pores, and the optimal aspect ratio of stiff pores is obtained by the least-square method using equations (A1) and (A2).

Step 2: The microcrack density at the different pressures is obtained by the least-square method. Then the moduli are obtained with equations (A3) and (A4).

Step 3: The relation between effective pressure and cumulative microcrack density is established.

$$\Gamma=\Gamma^{i}e^{-p/\hat{p}}, \tag{A5}$$

where Γ^{i} denotes the initial value when the effective pressure is zero, p is the pressure, and $\hat{p}$ is a constant.

Step 4: The microcrack aspect ratio distribution is computed. When the effective pressure increases, microcracks gradually tend to close. The minimum initial aspect ratio of the unclosed microcracks under effective pressure is determined by David and Zimmerman (2012)

$$\alpha_{p}^{i}=\frac{3}{4\pi}\int_{\Gamma^{i}}^{\Gamma}\frac{\left(1/K\left(\Gamma\right)-1/K_{eff}^{hp}\right)}{\Gamma}\frac{\mathrm{d}p}{\mathrm{d}\Gamma}d\Gamma, \tag{A6}$$

where $K(\Gamma)$ is the effective bulk modulus, which can be obtained by equation (A1).

Substituting equation (A4) into (A5), we obtain

$$\alpha_{p}^{i}=\frac{3}{4\pi}\int_{\Gamma}^{\Gamma^{i}}\frac{\left(1/K\left(\Gamma\right)-1/K_{eff}^{hp}\right)\hat{p}}{\Gamma^{2}}\mathrm{d}\Gamma, \tag{A7}$$

and by integrating equation (A6) from Γ to Γ^{i},

$$\alpha_{p}^{i}=\frac{4\hat{p}\left[1-\left(\upsilon_{eff}^{hp}\right)^{2}\ln\left(\frac{\Gamma^{i}}{\Gamma}\right)\right]}{3\pi K_{eff}^{hp}\left[1-2\upsilon_{eff}^{hp}\right]}, \tag{A8}$$

where $\upsilon_{eff}^{hp}=\left(3K_{eff}^{hp}-2G_{eff}^{hp}\right)/\left(6K_{eff}^{hp}+2G_{eff}^{hp}\right)$ is the effective Poisson ratio at the high effective pressures.

Based on equations (A4) and (A7), the relation between the minimum initial aspect ratio and the effective pressure can be obtained as

$$\alpha_{p}^{i}=\frac{4\left[1-\left(\upsilon_{eff}^{hp}\right)^{2}\right]p}{\pi E_{eff}^{hp}}, \tag{A9}$$

where $E_{eff}^{hp}=3K_{eff}^{hp}\left[1-2\upsilon_{eff}^{hp}\right]$ is the effective Young modulus at the high effective pressures. The cumulative microcrack density decreases with the effective pressure. If the effective pressure changes from zero to , the corresponding variation of cumulative crack density is . When the effective pressure increment is small enough, the variation of microcrack density can be considered to be caused by the closure of the microcracks with an aspect ratio less than the minimum initial aspect ratio. David and Zimmerman (2012) related microcrack porosity to microcrack density as

$$\phi_{c}=\frac{4\pi\alpha}{3}\Gamma. \tag{A10}$$

Therefore, the microcrack properties can be obtained based on the acoustic wave velocities as a function of the effective pressure from experimental measurements (Zhang et al., 2019).

Wu Chun-Fang obtained his Ph.D. degree from Hohai University in 2020. Her major is earth exploration and information technology, and her main research interests are rock physics and wave propagation theory in porous media.

Email: chunfang@hhu.edu.cn.